

## Highlights

### **A Machine Learning Approach to Automate Ductile Damage Parameter Selection in Finite Element Simulations**

A.N. O'Connor, P.G. Mongan, N.P. O'Dowd

- Bayesian optimisation derived parameters provide excellent agreement comparing simulated and experimental data.
- Ductile damage parameters are successfully derived for ambient and higher test temperatures.
- Required user-defined input such as test data can be easily generated from basic engineering tests.

# A Machine Learning Approach to Automate Ductile Damage Parameter Selection in Finite Element Simulations

A.N. O'Connor<sup>a,b</sup>, P.G. Mongan<sup>a,c</sup>, N.P. O'Dowd<sup>a,b,c</sup>

<sup>a</sup>*School of Engineering, University of Limerick, Ireland*

<sup>b</sup>*Bernal Institute, University of Limerick, Ireland*

<sup>c</sup>*Confirm Smart Manufacturing Research Centre, Ireland*

---

## Abstract

A key limitation of finite element analysis is accurate modelling of material damage. While additional material models exist that improve correlations between simulated damage and experimental data, these models often require additional parameters that are difficult to estimate. Here Bayesian optimisation, a machine learning technique, is shown to successfully identify material model parameters. The Bayesian derived material model parameters result in simulated output with less than 2 % error compared to experimental data. The framework detailed here is fully autonomous, requiring only basic information that can be derived from a simple tensile test. This framework has been successfully deployed to three datasets of P91 material tested at ambient (20 °C) and higher (500 °C) temperatures. Hyperparameters are shown to affect individual parameter values due to the ill-posedness of the problem.

*Keywords:* machine learning; bayesian optimisation; ductile damage;

---

*Email address:* `alison.oconnor@ul.ie` (A.N. O'Connor)

## 1. Introduction

The tensile test is a standard test method [1] that provides information about the mechanical properties of metallic materials. In cases where experimental data are limited finite element (FE) simulations can be used to simulate the mechanical behaviour of materials and examine hypotheses that cannot be experimentally investigated. The FE method offers a level of detail not obtainable from analytical solutions but is relatively computationally expensive and ultimately relies on experimental data for validation. Ductile damage modelling can be used in conjunction with FE simulations to represent mechanical behaviour of metals under high strain conditions when damage mechanisms are important [2–4]. Such models are generally complex and require calibration parameters that are difficult to derive experimentally or analytically. Calibrating a ductile damage modelling can be considered a form of “black box optimisation”, where the inputs (calibration parameters) and outputs (data in a tensile test) are known but the functional relationship between the calibration parameters and the material mechanical response is unknown. Such an optimisation problem can be solved using machine learning, a term used to describe algorithms and/or statistical models that allow computers to select the best method of progression in a problem, without human interaction or explicit programming [5]. In particular, Bayesian optimisation (BO) has been shown to outperform other machine learning algorithms in solving black-box optimisation problems [6]. Machine learning algorithms, informed directly by experimental and/or simulation data, have

been successfully employed to solve numerous engineering problems across a wide range of applications [7–9]. BO is commonly used in machine learning for artificial neural network (ANN) hyperparameter selection [5, 7, 10, 11] and has recently been used to identify material parameters in a viscoplastic material model, Ryan et al. [12]. The versatility of BO makes it an attractive method for solving a wide variety of engineering challenges such as: material design [13, 14], cardiac mechanics [15], light emission for thin films [16] and manufacturing process improvements [7, 17]. In [2, 3, 18, 19] ANNs have been used to assess damage model parameters. However, ANNs require a significant number of FE simulations to ‘train’ the model to recognise correlations and relationships between input values and results which is computationally expensive. This work demonstrates how BO can be used to automatically identify the material damage model parameters that best match experimental data from a tensile test, reducing the time associated with deriving parameter values and requiring minimal user intervention. A similar approach to that used in Ryan et al. [12] has been adopted, but in this case the approach is applied to ductile damage, using a Gurson model, rather than the rate sensitive viscoplasticity constitutive models examined in Ryan et al. [12].

## 2. Material behaviour in FE simulations

A tensile test consists of a standardised specimen geometry that is loaded in one direction until complete separation of the specimen. Data are typically expressed in terms of engineering stress and strain ( $\sigma_{eng}$  and  $\epsilon_{eng}$ , respectively), where stress and strain are derived from test measurements of

test machine load and specimen displacement, respectively. For metals the relationship between stress and strain typically comprises three regions (see Figure 1): a linear region, a strain hardening region where stress increases non-linearly with strain, and a material damage region where stress decreases non-linearly with increasing strain. Several key mechanical properties derived from a tensile test are illustrated in Figure 1. The yield strength ( $\sigma_y$ ) defines the stress at which material behaviour becomes non-linear. The linear region comprises data preceding the yield point of the material and the material stiffness or Young's modulus ( $E$ ) is the slope of the stress-strain curve, as shown in Figure 1. Beyond  $\sigma_y$  the slope of the stress-strain decreases and a local geometrical discontinuity known as a 'neck' forms in the tensile specimen. The ultimate tensile strength,  $\sigma_{UTS}$ , denotes the maximum stress reached in the tensile test; beyond which the specimen's load bearing capacity degrades. The strain hardening region occurs for  $\sigma_y \leq \sigma \leq \sigma_{UTS}$ , as illustrated in Figure 1, and depicts a non-linear stress-strain relationship. The conversion from a load-displacement curve to an engineering stress-strain curve (Equations 1 and 2) used in Figure 1, assumes that the specimen geometry does not change during the test.

$$\sigma_{eng} = \frac{P}{A} \quad (1)$$

$$\varepsilon_{eng} = \frac{\Delta l}{l_o} \quad (2)$$

Where  $P$  represents the force applied to the specimen,  $A$  the specimen cross-sectional area,  $\Delta l$  the change in length of the specimen and  $l_o$  the original length. However, as the specimen is stretched in the loading direction, in

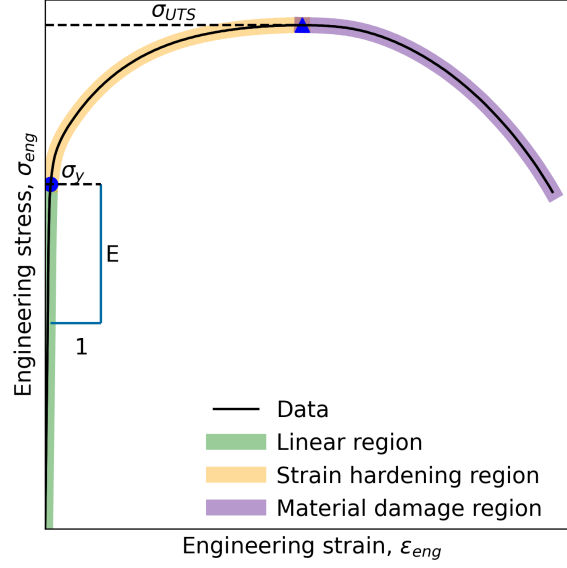


Figure 1: Illustration depicting material behaviour during tensile test experiment.

reduces in thickness in the direction transverse to the load, due to the Poisson effect [20]. Therefore, the cross-section area of the specimen decreases continuously with increasing load. To account for this geometric change a so-called true stress-true strain relationship (denoted as  $\sigma_{true}$  and  $\epsilon_{true}$ , respectively) is formulated from engineering stress-strain data, as shown in Equations 1 to 4 [20].

$$\sigma_{true} = \sigma_{eng} (1 + \epsilon_{eng}) \quad (3)$$

$$\epsilon_{true} = \ln(1 + \epsilon_{eng}) \quad (4)$$

This equation becomes increasingly inaccurate as the neck develops due to the non-uniformity of stress and strain in the neck. Therefore, in this work for  $\sigma > \sigma_{UTS}$ , the true stress is interpolated from the values for  $\sigma \leq \sigma_{UTS}$ ,

with the understanding that, in the absence of damage, the true stress always increases with increasing strain. Here, a linear relationship between true stress and true strain, with slope  $m$ , for  $\sigma \geq \sigma_{UTS}$  is assumed. The parameter  $m$  is unknown and is calibrated as part of the BO, as discussed later.

### 2.1. The damage model

A popular damage model, used to describe the softening behaviour seen in the material damage region of Figure 1, is the Gurson-Tvergaard-Needleman (GTN) model [3, 21, 22]. The parameters are typically estimated by conducting numerical simulations, manually iterating the relevant parameter value, and matching the simulation result to experimental data. The GTN model response for a tensile test is described in Equation 5, where  $\sigma$  is the current (uniaxial) stress,  $\sigma_y$  is the material yield strength,  $f$  is the current void volume fraction (the ratio of the volume of voids to the total material volume) and  $q_1$ ,  $q_2$ , and  $q_3$  are material parameters,

$$\left(\frac{\sigma}{\sigma_y}\right)^2 + 2q_1f \left(\cosh \frac{q_2\sigma}{2\sigma_y}\right) - q_3f^2 = 1. \quad (5)$$

The rate of change of the void volume fraction,  $f$ , is described by Equation 6 where  $\dot{f}_n$  and  $\dot{f}_g$  represent the void nucleation rate and void growth rate, respectively.

$$\dot{f} = \dot{f}_n + \dot{f}_g \quad (6)$$

The void growth rate,  $\dot{f}_g$ , is obtained from conservation of mass,

$$\dot{f}_g = (1 - f)\dot{\epsilon}, \quad (7)$$

while the void nucleation rate,  $\dot{f}_n$ , is given by Equation 8, where  $\varepsilon_m^p$  is the plastic strain of the unvoided (matrix) material, and  $f_N$ ,  $S_N$  and  $\varepsilon_N$ , are material parameters.

$$\dot{f}_n = \frac{f_N}{S_N \sqrt{2\pi}} \exp \left[ -\frac{1}{2} \left( \frac{\varepsilon_m^p - \varepsilon_N}{S_N} \right)^2 \right] \dot{\varepsilon}_m^p, \quad (8)$$

Since, the void volume,  $f$ , is defined through a rate equation, the initial void volume fraction,  $f_0$ , must also be defined. Hence, there are a total of seven parameters in the GTN ductile damage model to fit using BO:  $q_1$ ,  $q_2$ ,  $q_3$ ,  $S_N$ ,  $f_N$ ,  $\varepsilon_N$ , and  $f_0$ . Including the slope of the true stress-true strain curve for  $\sigma > \sigma_{UTS}$ ,  $m$ , gives a total of eight parameters.

### 3. The Bayesian Optimisation Framework

The goal of BO is to find the global minimum of an unknown (black box) function. There are two key ingredients to a BO framework: a surrogate model and a loss function which work jointly with an acquisition function. The surrogate model, sometimes called a probabilistic model, describes the BO's current knowledge about the unknown function based on observed data. The loss function describes how well the previously observed data are optimised (i.e. converging towards a global minimum) [23]. The acquisition function controls how the BO explores the parameter space.

*'A Gaussian process is defined as a collection of random variables'* [24] many of which have consistent, joint Gaussian distributions, that are specified by the covariance function [25]. Gaussian process regression (GPR) uses Gaussian processes theory to define a surrogate model  $f(x)$  based on regression of limited inputs  $x$ . To generate a surrogate model, observed data about



the unknown function must be provided to the BO framework.

The covariance function (also referred to as kernel, covariance kernel or kernel function), is user-defined and the choice of the covariance function has significant impact on the GPR and, by extension, the overall BO result [26]. For black-box functions where the shape and characteristics are unknown it is common to combine multiple covariance functions to provide a wide-range of characteristics that might be relevant to the unknown function.

The probability distribution generated by GPR is based on a ranking system, where input  $x$  is evaluated as  $f(x)$ . The evaluation,  $f(x)$ , is then ranked in terms of its performance relative to the loss function. In this work the loss function is the mean average percentage error (MAPE) which quantifies the similarity between simulated and experimental data (see Section 3.2 for further detail). To minimise the loss function the L-BFGS-B optimisation algorithm [27] is used. This algorithm uses historical gradient evaluations to build up an approximation of the unknown function. The L-BFGS-B algorithm is popular for large scale optimisation problems as it requires less memory compared to other methods.

In this implementation of BO optimisation, the method repeats until either a suitable solution has been found (MAPE is below a specified value) or, some maximum number of iterations has been carried out.

In order to set reasonable bounds to the possible solutions of the problem, a parameter space is defined, within which the BO algorithm will search for relevant values. The parameter space of this problem is defined in Table 1 for the GTN parameters, based on information in the literature for similar materials [28–30]. The minimum value of parameter  $m$  is assumed to be

zero, which corresponds to no strain-hardening. The process used to define the bounds for  $m$  is outlined in detail in Section 4.

Table 1: Parameter space representing the minimum and maximum boundary for each parameter

Dataset	Parameter	Minimum	Maximum
1-3	$q_1$	$9.00 \times 10^{-1}$	1.60
1-3	$q_2$	$9.00 \times 10^{-1}$	1.10
1-3	$q_3$	$8.10 \times 10^{-1}$	2.56
1-3	$\epsilon_N$	$2.50 \times 10^{-1}$	$4.00 \times 10^{-1}$
1-3	$f_N$	$3.00 \times 10^{-1}$	$9.00 \times 10^{-2}$
1-3	$s_N$	$1.00 \times 10^{-1}$	$2.00 \times 10^{-1}$
1-3	$f_0$	$1.30 \times 10^{-3}$	$1.50 \times 10^{-3}$
1	$m$	0	800
2	$m$	0	1100
3	$m$	0	800

### 3.1. The covariance function

The covariance function used in the GPR has significant influence on the shape and characteristics of the surrogate function [7]. In this work a covariance function,  $k(x_i, x_j)$ , using a combination of the Matérn, Constant and White noise (White) functions, as shown in Equation 9, is implemented.

$$k(x_i, x_j) = \text{Matérn} + \text{Constant} \times \text{White} \quad (9)$$

The Matérn covariance function is defined in Equation 10 [31],

$$k(x_i, x_j) = \frac{1}{\Gamma(\nu) 2^{\nu-1}} \left( \frac{\sqrt{2\nu}}{l} d(x_i, x_j) \right)^\nu K_\nu \left( \frac{\sqrt{2\nu}}{l} d(x_i, x_j) \right). \quad (10)$$

In Equation 10  $d(\cdot, \cdot)$  is the Euclidean distance,  $K_\nu(\cdot)$  is a modified Bessel function and  $\Gamma(\cdot)$  is the gamma function.

To modify the mean of the Gaussian process the Constant covariance function see Equation 11 [31] is used.

$$k(x_i, x_j) = C; \forall x_i, x_j, \quad (11)$$

where  $C = 1.0$  is a constant. The White noise covariance function allows users to more accurately model noisy data. The White covariance function is defined in Equation 12, where  $x_i$  and  $x_j$  are input points,  $\sigma^2$  is the variance of the noise and  $\delta_{ij}$  the Kronecker delta function.

$$k(x_i, x_j) = \sigma^2 \delta_{ij} \quad (12)$$

As the shape and/or characteristics of the black-box function are unknown the covariance kernel (Equation 9) is designed to account for shifts in mean position (Constant), noise (White) and to model potentially multiple minima positions (Matérn). In this work hyperparameters are fixed:  $\nu = 1$ ,  $l = 1$ ,  $C = 1$ ,  $\sigma^2 = 1$  with the bounds, for each kernel hyperparameter, restricted to:  $(1 \times 10^{-5}, 1 \times 10^5)$ .

### 3.2. The loss function

The aim of this work is to minimise the difference between experimental test data and simulation outputs generated from FE. The experimental data

are measures of applied load and specimen extension taken in-situ. Simulated data, comparable to experimental data measures, are extracted from each FE simulations (see Section 5 for further detail). In this work mean average percentage error (MAPE), Equation 13, is used to measure the similarity between experimental data and simulated output.

$$\text{MAPE} = \frac{100}{n} \sum_i^n \left| \left[ \frac{P_{exp}^i - P_{sim}^i}{P_{exp}^i} \right] \right|. \quad (13)$$

Here  $P_{exp}^i$  represents each experimental load data point,  $P_{sim}^i$  the corresponding simulation load and  $n$  the number of data points. MAPE provides an average measure of error over the full dataset. All data points are equally weighted. To ensure that the values of  $P_{exp}^i$  and  $P_{sim}^i$  correspond to the same displacement the following procedure is implemented: The smallest change in displacement ( $\Delta u_{min}$ ) in the full set of experimental or simulated data points is identified. Both experimental and simulated arrays are interpolated assuming a cubic relationship with an increment of  $\Delta u_{min}$ . The corresponding experimental and simulated loading values  $P_{exp}^i$  and  $P_{sim}^i$  are then directly compared using Equation 13 to calculate similarity.

### 3.3. The acquisition function

In this work the upper confidence bound (UCB) acquisition function is employed. The UCB identifies the new parameters through a weighted sum of the surrogate function,  $\mu(x)$ , and the uncertainty,  $\sigma(x)$ , [23, 32] as shown in Equation 14.

$$\alpha_{UCB}(x) = \mu(x) + \sqrt{B_t} \sigma(x). \quad (14)$$

When the weight,  $\sqrt{B_t}$ , is large the acquisition function operates in “exploratory” mode; reducing the weight switches the model to “exploitation” mode. Exploration and exploitation balance how the model searches the parameter space. In exploration mode the new assessment point differs significantly compared to that of the previous iteration; exploratory mode returns a new assessment point more similar to that tested previously. The trade-off between exploration and exploitation is two-fold. Firstly it ensures that the model produces results in a reasonable timescale but secondly, and somewhat more importantly, the trade-off ensures the model doesn’t fall into a local minima. In this research the complexity of the BO framework is minimised by fixing  $B_t = 2.5$ .

### *3.3.1. Acquisition function hyperparameters*

The values of the acquisition function hyperparameters can have a significant impact on model performance [6, 11]. In addition to the weight,  $B_t$ , the acquisition function has two further hyperparameters: The number of random samples,  $N_R$ , and the number of optimisation samples,  $N_O$ .  $N_R$  controls the size of the array over which the range of possible inputs are distributed. The main influence of  $N_R$  is in calculating the mean of the black-box function. Increasing  $N_R$  increases the precision of the GPR, thus reducing uncertainty.  $N_O$  defines how many evaluations of the acquisition function are conducted and controls the level of uncertainty in the acquisition function. Increasing  $N_O$  makes the optimisation process more robust.

Table 2: Design of experiments array for 8 parameters with each parameter at 2 levels.

	$P_1$	$P_2$	$P_3$	$P_4$	$P_5$	$P_6$	$P_7$	$P_8$
<b>1</b>	1	1	1	1	1	1	1	1
<b>2</b>	1	1	1	1	1	2	2	2
<b>3</b>	1	1	2	2	2	1	1	1
<b>4</b>	1	2	1	2	2	1	2	2
<b>5</b>	1	2	2	1	2	2	1	2
<b>6</b>	1	2	2	2	1	2	2	1
<b>7</b>	2	1	2	2	1	1	2	2
<b>8</b>	2	1	2	1	2	2	2	1
<b>9</b>	2	1	1	2	2	2	1	2
<b>10</b>	2	2	2	1	1	1	1	2
<b>11</b>	2	2	1	2	1	2	1	1
<b>12</b>	2	2	1	1	2	1	2	1

### 3.4. Initialising the BO framework

BO requires a database of initial evaluated data. A design of experiment (DoE) approach is used, [33, 34], to provide the initial evaluated data within the parameter space. DoE essentially maximises the statistical significance of results with a minimised number of experiments or, as in this case, a minimised number of virtual experiments (i.e. FE simulations). Table 2 shows a DoE array for 12 initial simulations based on the maximum and minimum parameter space values, where values of 1 and 2 in Table 2 represent the minimum and maximum parameter bounds, respectively.

Figure 2 shows a flowchart describing the DoE procedure. The user defines the parameter space. A DoE array, such as that shown in Table 2, is input. The DoE array is then modified so that the minimum and maximum values are replaced by the user-defined parameter space values. A FE simulation for each row of the DoE array, such that  $i_{max}$  is the number of rows in the DoE array, is conducted. Results from the simulation are processed to extract the force and displacement of relevant elements. The physical experiment data are compared to the simulation data, and an error measurement is calculated (see Section 3.2 for further detail). After each iteration parameter values and the associated error measurement are appended to a csv file.

### 3.5. The Bayesian Optimiser

The output of the DoE (a csv file of parameter values and error measurements, Figure 2) is used to initialise the Bayesian optimiser. Figure 3 diagrammatically details the method applied. DoE data are analysed by the GPR to create an initial surrogate model. GPR outputs are provided to the acquisition function which identifies new parameter values based on ranking the DoE data. A new simulation, using acquisition function parameter values, is then conducted. Again simulation data is compared to the experiment and an error calculated. Acquisition function parameter values and error measurement data are appended to the existing csv file. To assess whether the model should exit several operations, collectively referred to as a termination function, are conducted. In the current analysis, to avoid system exit prior to the application of BO, the DoE values are not included as part of the termination function. As shown in Figure 3 the algorithm will iterate until the termination function recognises that an appropriate solution

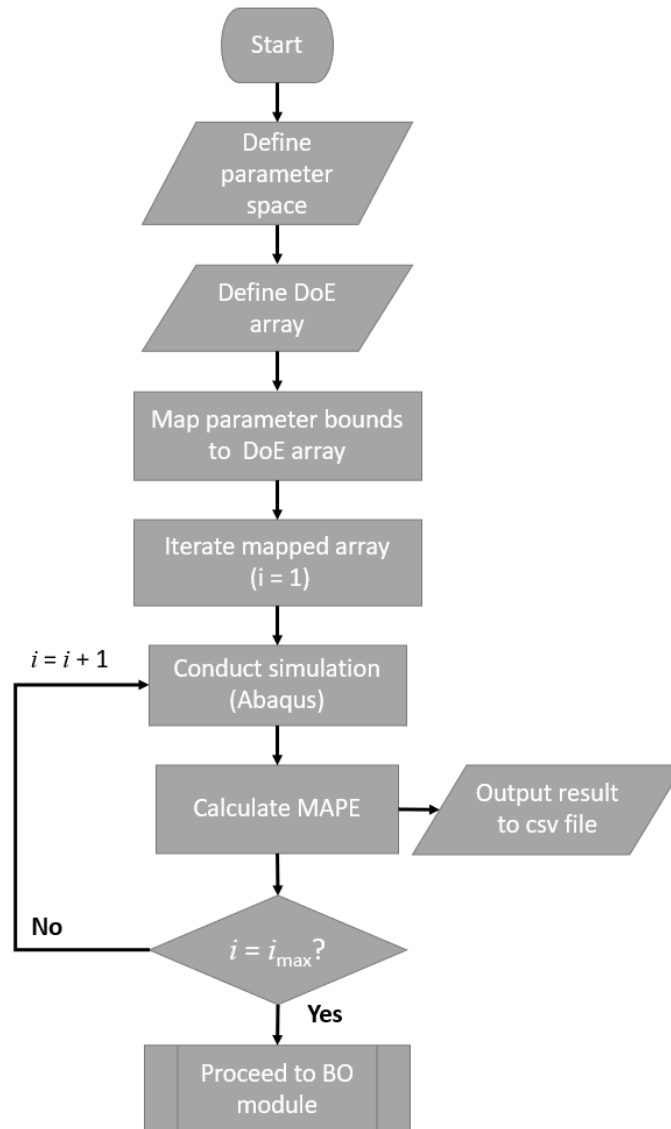


Figure 2: Flowchart demonstrating the design of experiments code procedure (prior to bayesian optimisation).



is found (i.e. error of less than 2 % when comparing simulated and experimental results) or a maximum number of iterations ( $j_{max}$ ) is achieved. The iteration number  $N_j$  at which a solution was found is identified.

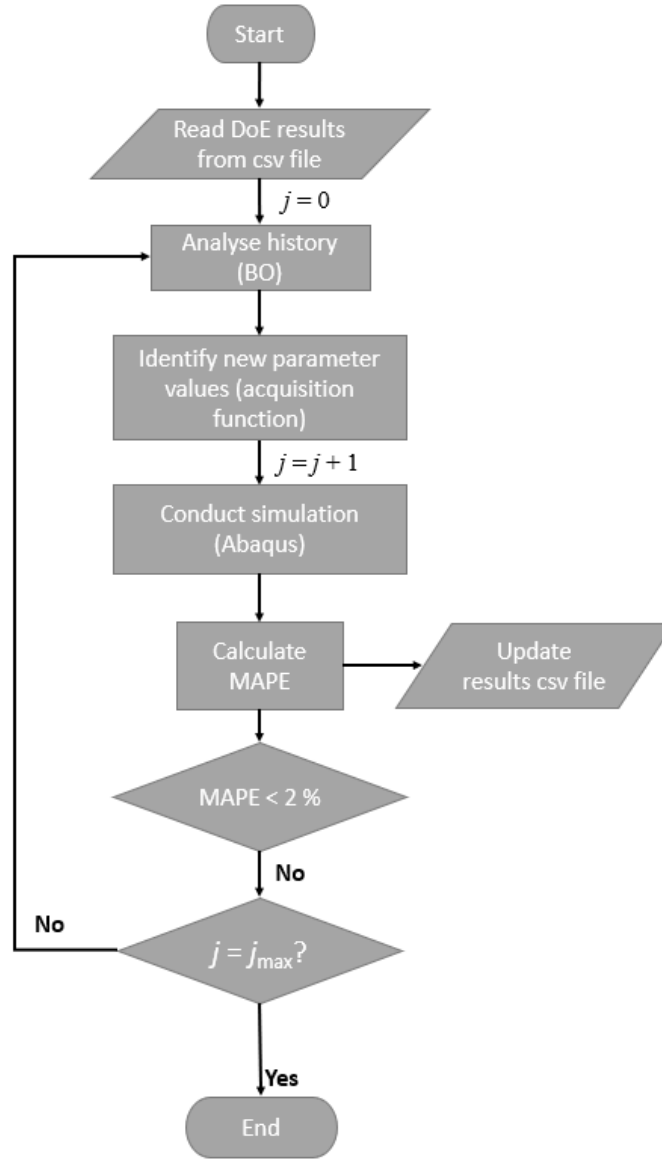


Figure 3: Flowchart depicting code procedure for Bayesian optimisation.

#### 4. Experimental Tensile Tests

The three experimental tensile test results are shown in Figure 4 for the material of interest (P91, a piping steel). Datasets 1 & 2 were conducted under identical test conditions. Therefore Dataset 2 can be considered a ‘repeat’ test result. Load-displacement data were converted to true stress-

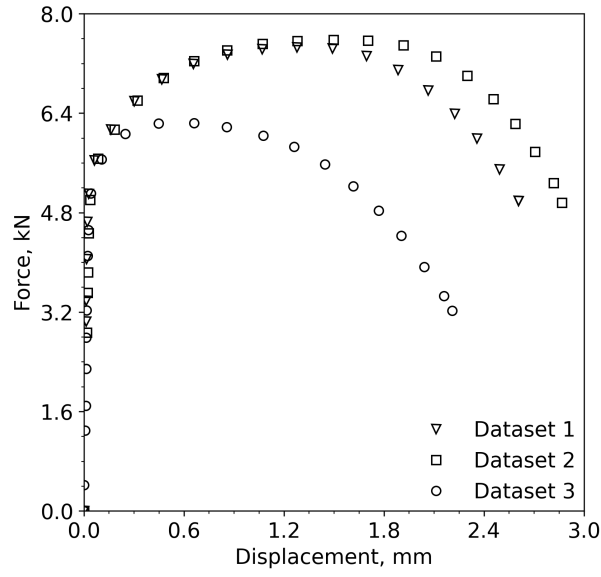


Figure 4: Experimental tensile test results for P91 material at test temperatures of 20 °C (Datasets 1 and 2) and 500 °C (Dataset 3). Note: Markers are placed as specific intervals for data visibility purposes. Higher data acquisition rate was used during testing.

strain by limiting data to the range below the maximum load.

The ultimate tensile strength ( $\sigma_{UTS}$ ) was defined as the true stress corresponding to the maximum load. The second derivative of true strain was calculated using a Savitzky-Golay filter with a three degree polynomial fit.

#### 4.1. Assessment of linear data

To ensure the yield strength was accurately defined the size of the filter window (i.e. the number of data points over which the polynomial is applied) was solved iteratively. For each iteration (i.e. each window size) the yield strength ( $\sigma_y$ ) was defined as the position of the inflection point. The ‘best’ yield strength was selected as a function of the error (between the predicted linear region and the experimental linear region), the overall fit of the linear region ( $r^2$ ) and the estimated yield strength value. Young’s modulus was calculated by employing linear regression to fit all data below the proposed ‘best’ yield strength. Figure 5 shows the result of the assessment for each of the three datasets.

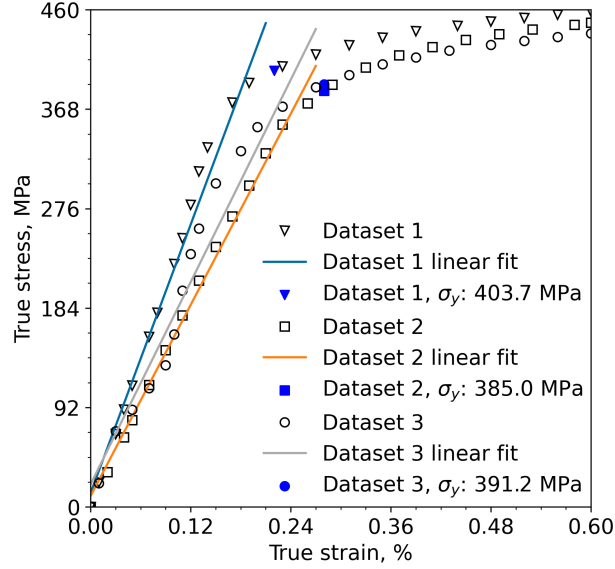


Figure 5: True stress - true strain relationship for three experimental tests.

To extrapolate data beyond  $\sigma_{UTS}$  a linear relationship between stress and strain was assumed. The slope of the extrapolated line, parameter  $m$ , is a

searchable parameter that the BO framework will derive. The maximum value of parameter  $m$  was ascertained from experimental data by applying a linear fit to groups of data preceeding the  $\sigma_{UTS}$  position. The first fit was applied to a single pair of data points immediately adjacent to the  $\sigma_{UTS}$  position, the second fit was applied to the previous pair plus an additional data point, the third fit was applied by expending the second group by an additional data point and so on. This method was applied up to a maximum of five data points preceding the  $\sigma_{UTS}$  position. Parameter  $m$  was assessed for each linear fit and the largest value was selected to represent the maximum parameter boundary. True stress-true strain data were extrapolated based on the assumption that the extrapolated line must pass through the  $\sigma_{UTS}$  position with a slope of parameter  $m$ . Figure 6 shows the extrapolated data for the parameter space of dataset 1.

## 5. FE Modelling of Tensile Tests

Finite element modelling was conducted using Abaqus 2021 [30]. Analyses were conducted using Abaqus/Explicit, a dynamics based solution, with a mass scaling factor of 10 to reduce computation time. The model was meshed using axisymmetric elements. A total of 4664 elements were used. Each element in the gauge section represents approximately 0.09 mm.

The experimental tensile test geometry was represented as shown in Figure 7. The use of a 2D geometry reduces the computational expensive associated with the simulation. To predispose the FE model to neck in the central gauge length a small imperfection was introduced to the bottom right hand corner as shown in Figure 7.

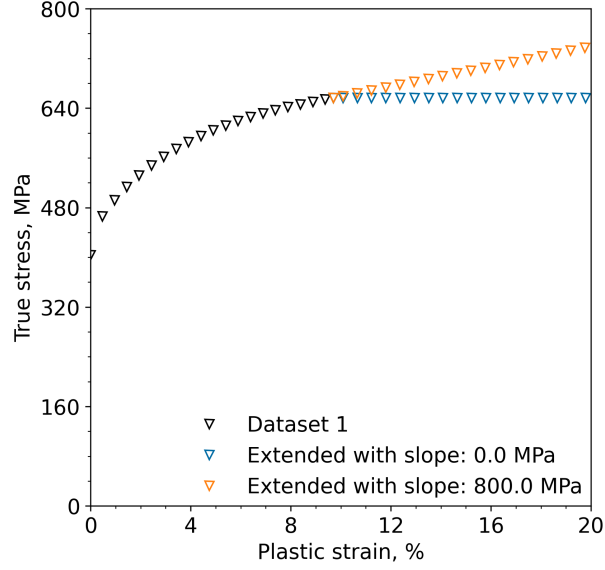


Figure 6: True stress - plastic strain relationship for dataset 1. Test data are shown using black markers. Two parameter values (minimum and maximum) are distinguished using coloured markers.

Boundary conditions were applied along the symmetry planes (shown by the red dashed lines in Figure 7). A reference node (red point shown in Figure 7) was coupled to the surface of the geometry and loading was applied through displacement control.

Within the FE simulation linear material behaviour was defined using the  $E$  and Poisson's Ratio ( $\nu = 0.3$ ). Non-linear material behaviour was provided as an array of plastic strain versus true-stress (\*PLASTIC in Abaqus). To model material degradation due to ductile damage the GTN model was applied (see Section 2.1).

Displacement data was taken from the reference node shown in Figure 7. The applied load was calculated by summing the vertical reaction force in

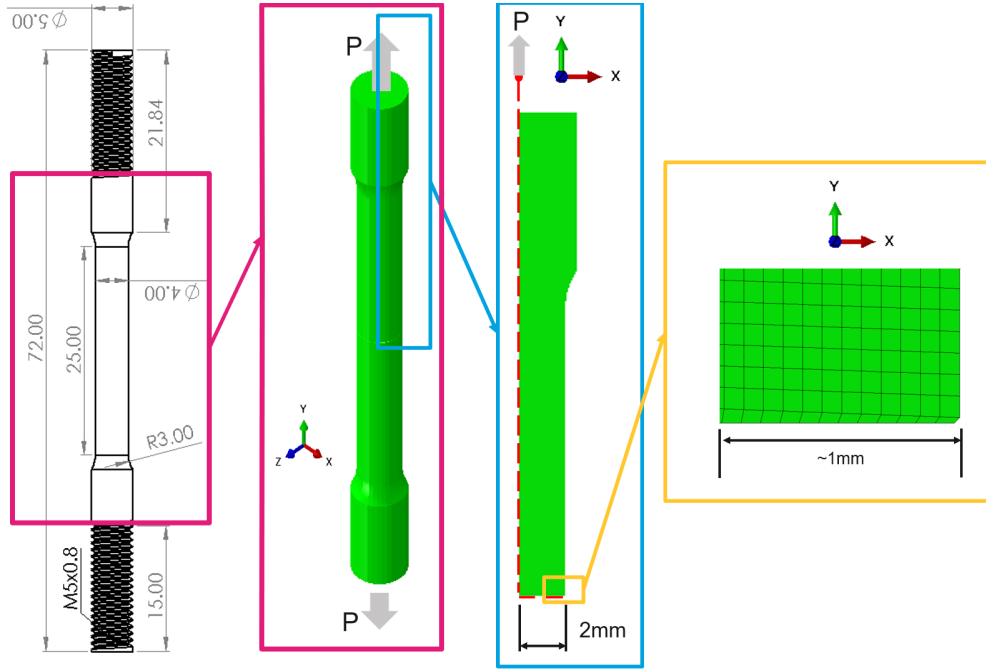


Figure 7: Illustration demonstrating the axisymmetric FE model. A small imperfection, shown in the yellow highlighted region, was modelled to ensure failure occurred in the midsection of the gauge length.

elements located along the X symmetry plane.

## 6. Results and Discussion

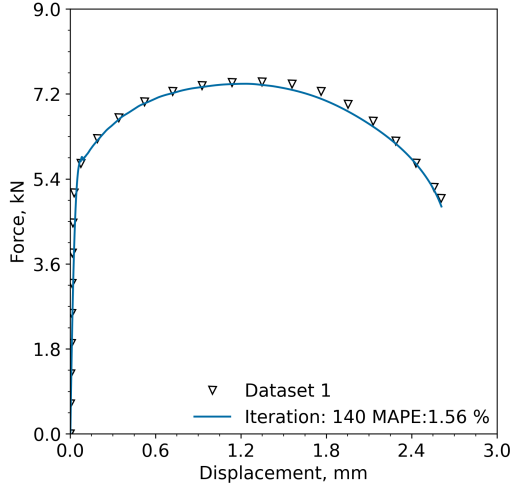
As discussed, three data sets have been analysed. The minimum MAPE selected is 2% and the procedure described in Figure 3 is applied until this MAPE is reached. Abaqus simulations are preformed in sequence with 4 CPUs. Typically, this framework requires at least 150 finite element simulations with the full parameter selection taking approximately 4 hours. The framework was executed on a laptop with 4 Intel i7 CPUs and 32 gigabytes of RAM. Not all CPUs are required for the framework, other applications

(e.g. Microsoft office) are sufficiently supported while the framework runs in the background. The lowest MAPE, 1.56 %, was found for dataset 1.

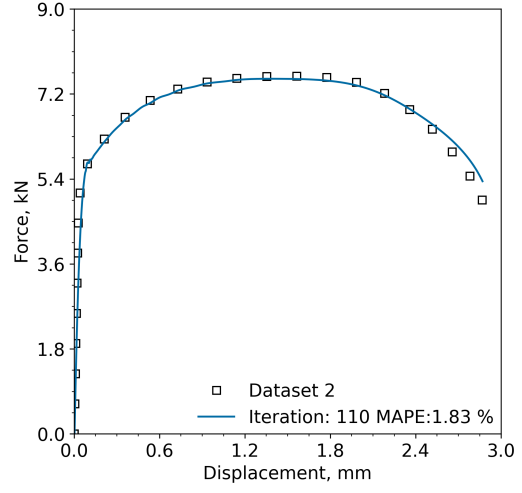
The comparison between data and simulation is shown in Figure 8 for the three datasets. Figure 8a shows that the simulated output is in good agreement with experimental data over the full displacement range although simulated forces are slightly underestimated compared with the experiment in the range  $1.3 \leq \Delta u \leq 2.2$  mm. Similarly Dataset 2 (Figure 8b) shows good agreement between simulated and experimental data. For  $\Delta u \geq 2.5$  mm simulated results for Dataset 2 slightly overestimate the force compared to the experiment. The overestimation is most notable at the final displacement point.

The parameter values selected by the BO framework are provided in Table 3 for each of the three datasets analysed.

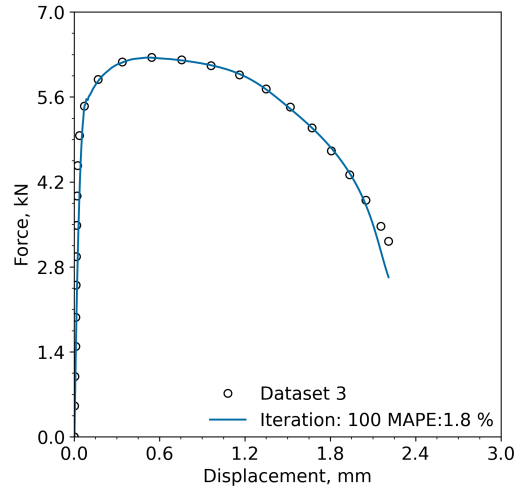
The datasets analysed are for the same batch of material. The tests for dataset 1 and 2 have been carried out under identical conditions, while the test for dataset 3 has been carried out at a different temperature. The statistical nature of materials testing, often termed material scatter, has been widely acknowledged in the field of material science [35]. Given the difficulty in experimentally deriving material values and considering the statistical nature of material performance, it may be that machine learning methods such as the ones employed here are more appropriate for defining such parameters. It is interesting to note that parameter  $m$ , the slope of the extrapolated true stress-true strain curve was found to differ significantly between datasets 1 and 2. The optimised parameter  $m$  for datasets 1 was found to be 534 MPa while that for dataset 2 was found to be 725 MPa. Both datasets were tested



(a) Dataset 1



(b) Dataset 2



(c) Dataset 3

Figure 8: Comparison of experimental test data to simulated output for Dataset 1 (8a), Dataset 2 (8b), and Dataset 3 (8c). Parameter values are shown in Table 3.



Table 3: Bayesian optimisation framework parameter values for each of the three datasets analysed.

Parameter	Dataset 1	Dataset 2	Dataset 3
$N_O$		500	
$N_R$		50,000	
$q_1$	1.332	1.168	1.182
$q_2$	$9.952 \times 10^{-1}$	$9.667 \times 10^{-1}$	$9.699 \times 10^{-1}$
$q_3$	2.295	1.407	2.001
$\epsilon_N$	$2.900 \times 10^{-1}$	$3.467 \times 10^{-1}$	$3.720 \times 10^{-1}$
$s_N$	$1.671 \times 10^{-1}$	$1.856 \times 10^{-1}$	$1.214 \times 10^{-1}$
$f_N$	$3.869 \times 10^{-2}$	$8.481 \times 10^{-2}$	$4.706 \times 10^{-2}$
$f_0$	$1.370 \times 10^{-3}$	$1.340 \times 10^{-3}$	$1.310 \times 10^{-3}$
$m$	534.1	725.4	421.4
MAPE	1.563	1.827	1.799
$N_j$	140	110	100

under identical conditions and, as shown in Figure 4, are broadly similar up to a displacement of  $\approx 1.3$  mm after which they begin to diverge.

It is also interesting to note that for all three datasets the parameter  $f_0$ , representing the initial void volume fraction of the material are very similar. Generally the initial void volume fraction is assumed to be applicable to all test samples taken from a single batch of material which is consistent with what is observed here. However, comparing parameters  $\epsilon_N$ ,  $s_N$  and  $f_N$  across the three datasets presented in Table 3, there are significant dif-

ferences. These parameters control how many voids nucleate under a given loading condition and, as such, are expected to be material specific rather than specimen specific.

In terms of the fitting parameters ( $q_1$ ,  $q_2$  and  $q_3$ ) it is common practise among the engineering community to fix  $q_3 = q_1^2$  [36–38] this is based on assumptions made in the original model [39]. In this work  $q_3$  was not constrained as a function of  $q_1$ . Interestingly, despite the freedom of the BO framework to select any value of  $q_3$ , Table 3 shows that dataset 2 found a value of  $q_3 = 1.4071$  which is analogous to  $q_1^2 = 1.3652$ . Other fitting parameters ( $q_1$  and  $q_2$ ) are broadly similar when comparing across datasets. Given the complex nature of the material model and the close relationship between some parameters it is difficult to state with any certainty what impact any individual parameter has had on simulated output.

### 6.1. Effect of varying BO hyperparameters

To assess the effect of hyperparameter selection on the model parameters multiple analyses on dataset 1 were preformed. For each analysis the number of random and/or optimisation samples ( $N_R$  and  $N_O$ , respectively) were reduced as shown in Table 4. Reducing  $N_R$  reduces the precision of the input parameters which increases model uncertainty. The  $N_O$  defines how many evaluations of the acquisition function are conducted, this controls the level of uncertainty specifically related to the acquisition function. Results are plotted in Figure 9.

Figure 9 shows that excellent agreement with experimental data is achieved for the four different hyperparameter choices but, it may be noted from Table 4 that the model parameters can depend significantly on hyperparameter

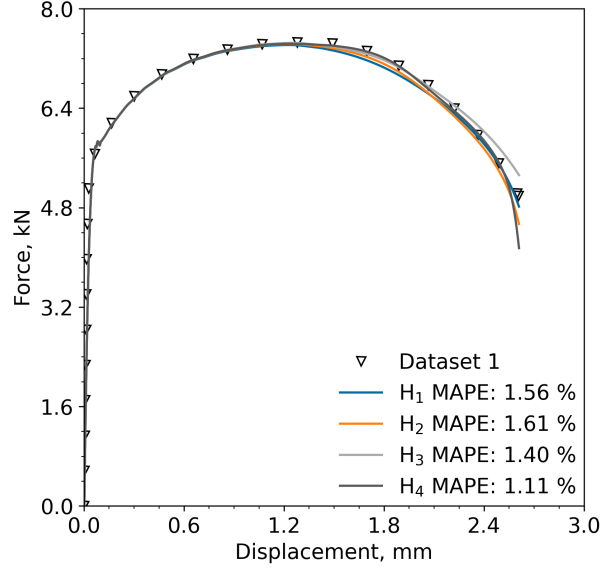


Figure 9: Plot of force versus displacement showing experimental data and simulated output for various hyperparameters.

selection. Given that excellent agreement was achieved for all four analyses this implies that the problem does not have a unique solution. That is to say that multiple combinations of the eight model parameters potentially provide good agreement to experimental data.

The lowest MAPE, 1.11 % was found for analysis  $H_4$  where  $N_R$  and  $N_O$  were 10,000 and 100, respectively. Comparing the model parameters ( $q_1$ ,  $q_2$  etc.) for the four analyses shows that  $H_4$  deviates considerably from  $H_1$ .  $H_1$ , as it has the highest  $N_R$  and  $N_O$ , is considered the most precise of the analyses investigated here. Comparing parameter  $m$  in analyses  $H_1$  (534.13 MPa) and  $H_4$  (621.85 MPa) shows a difference of almost 100 MPa. In terms of the expected change, and considering the parameter range, the deviation across analyses is significant. It is therefore not unexpected that

Table 4: Bayesian optimisation framework parameter values for dataset 1. The effect of hyperparameter settings on GTN parameter values.

Parameter	$H_1$	$H_2$	$H_3$	$H_4$
$N_O$	500	100	500	100
$N_R$	50,000	50,000	10,000	10,000
$q_1$	1.332	1.178	1.291	1.158
$q_2$	$9.952 \times 10^{-1}$	1.021	$9.547 \times 10^{-1}$	1.037
$q_3$	2.295	1.344	2.254	1.070
$\epsilon_N$	$2.900 \times 10^{-2}$	$3.598 \times 10^{-1}$	$3.519 \times 10^{-1}$	$3.331 \times 10^{-1}$
$s_N$	$1.671 \times 10^{-1}$	$1.580 \times 10^{-1}$	$1.001 \times 10^{-1}$	$1.234 \times 10^{-1}$
$f_N$	$3.869 \times 10^{-2}$	$5.769 \times 10^{-2}$	$3.086 \times 10^{-2}$	$7.594 \times 10^{-2}$
$f_0$	$1.370 \times 10^{-3}$	$1.431 \times 10^{-3}$	$1.412 \times 10^{-3}$	$1.309 \times 10^{-3}$
$m$	534.1	542.8	514.5	621.9
MAPE	1.563	1.614	1.398	1.105
$N_j$	140	133	46	130

the remaining parameter values, those specific to the GTN model, also differ. This outcome supports the non-uniqueness of the problem.

Comparing  $H_1$  and  $H_2$  in Table 4 indicates how reducing  $N_O$  affects the analysis. While individual model parameters change slightly, overall both analyses provide similar measures of MAPE and result in load-displacement traces similar to the experimental data (Figure 9). It should be noted that  $H_2$  resulted in a slightly higher MAPE, 1.61 %, compared to that of  $H_1$ , 1.56 %. The higher measure of MAPE for  $H_2$  is as expected given that the

reduced  $N_O$  effectively reduces the amount of statistical information known about the black-box function resulting in less accuracy.

Comparing  $H_1$  and  $H_3$  in Table 4 enables the effect of reducing  $N_R$  to be assessed. Here it is shown that fitting parameters  $q_1$ ,  $q_2$  and  $q_3$  are broadly similar. Other parameters, specifically nucleation related terms  $s_N$  and  $f_N$ , exhibit differences with  $H_3$  having smaller values compared to  $H_1$ . The effect of the reduction in these parameters is also notable in Figure 9 where comparing  $H_1$  and  $H_3$  shows that  $H_3$  deviates from  $H_1$  at  $2.0 \leq \Delta \leq 2.7$  mm. In essence the lower nucleation parameters seen in analysis  $H_3$  reduced the nucleation of new voids thus giving a lower rate of damage compared to  $H_1$ . On the whole comparing  $H_1$  and  $H_3$  indicates that reducing  $N_R$  did not significantly affect the model output. In fact comparing  $H_1$  and  $H_2$  to  $H_3$  shows that lower  $N_R$  provided a more accurate result (i.e. lower MAPE) in a significantly shorter timescale (iteration number 46). While this may appear initially surprising it simply means that lower values of  $N_R$  did not overtly effect the mean calculation of the block-box function. Analysis  $H_4$  shows output associated with a reduction in both the  $N_O$  and  $N_R$ . Interestingly  $H_4$  has the lowest MAPE, 1.11 %, however the number of iterations (130) is similar to those required for the  $H_1$  and  $H_2$  analyses.

It is difficult to state with any certainty which, if any, of the analyses in Table 4 would be considered the most ‘appropriate’. The issue of non-uniqueness in GTN model parameter values has been highlighted by others [3, 28]. One method of limiting the GTN parameters is to introduce other, cracked, specimen geometries such as single edge notch bend (SENB) or compact tension (CT) geometries. Cracked geometries are subject to

considerable local stress triaxiality that inhibits plastic flow and promotes void growth [40]. As the GTN model, Equation 5, is not specimen specific the parameters of the model should be equally applicable to a uni-axial tensile geometry or a fracture toughness geometry (e.g. SENB or CT geometry). Theoretically one could integrate several types of geometry to the framework developed here to limit the number of parameter combinations. However, the introduction of a cracked geometry causes several complications. Numerical simulations of cracked geometries often require contact interactions and specialist meshing techniques which increases model complexity and computational demand. While this is certainly within the ability of modern computing ability the increase in computational demand would inevitably increase the required time for BO to define a solution. Testing cracked geometries typically requires additional material, expensive and specialist laboratory equipment and expertise in fracture mechanics. Where test data are not available the loss function (MAPE) for the cracked geometry cannot be calculated leaving the BO framework, specifically the acquisition function, struggling to rank data.

## 7. Conclusions

- Bayesian optimisation framework successfully derived an array of 8 parameter values that, when applied to a ductile damage model simulation, produced an accurate representation of experimental data with a mean average percentage error of less than 2 %.
- The framework is fully autonomous requiring only basic information that can be easily generated from experimental tensile test data.

- GTN model parameter values are non-unique and it is shown that multiple combinations provide excellent agreement to experimental data.
- GTN model parameter values are affected by changes to the acquisition function hyperparameters.

A preprint of this research is available [41]. Additional supplementary information such as data files and code are available from GitHub [https://github.com/alisonoc/PAPER\\_A](https://github.com/alisonoc/PAPER_A).

## 8. Acknowledgements

This work was funded by the European Union through the Marie Skłodowska-Curie Actions grant number 101028291. William Brennan, a University of Limerick undergraduate, is thanked for his contributions to earlier versions of the algorithm used in this work. We gratefully acknowledge helpful conversations with Dr. Meghana Kshiragar and Gauri Vaidya from the University of Limerick’s Lero Centre. We also thank the Mathematics Applications Consortium for Science and Industry (MACSI) group for their insightful and supportive comments surrounding this research.

## References

- [1] EN ISO 6892-1:2019 Metallic materials - Tensile testing - Part 1: Method of test at room temperature (ISO 6892-1:2019), 2019.
- [2] F. Abbassi, T. Belhadj, S. Mistou, A. Zghal, Parameter identification of a mechanical ductile damage using Artificial Neural Networks in sheet

- metal forming, *Materials & Design* 45 (2013) 605–615. doi:<http://dx.doi.org/10.1016/j.matdes.2012.09.032>.
- [3] Y. Chahboub, S. Szavai, Determination of GTN parameters for SENT specimen during ductile fracture, in: *Procedia Structural Integrity*, volume 16, Elsevier B.V., 2019, pp. 81–88. doi:[10.1016/j.prostr.2019.07.025](https://doi.org/10.1016/j.prostr.2019.07.025).
- [4] T. Zhang, K. Lu, A. Mano, Y. Yamaguchi, J. Katsuyama, Y. Li, A novel method to uniquely determine the parameters in Gurson–Tvergaard–Needleman model, *Fatigue & Fracture of Engineering Materials & Structures* 44 (2021) 3399–3415. doi:[10.1111/ffe.13568](https://doi.org/10.1111/ffe.13568).
- [5] T. Bismukhametov, J. Jäschke, Combining machine learning and process engineering physics towards enhanced accuracy and explainability of data-driven models, *Computers & Chemical Engineering* 138 (2020) 106834. doi:[10.1016/j.compchemeng.2020.106834](https://doi.org/10.1016/j.compchemeng.2020.106834).
- [6] J. Snoek, H. Larochelle, R. P. Adams, Practical Bayesian Optimization of Machine Learning Algorithms, in: *Advances in Neural Information Processing Systems*, volume 25, Curran Associates, Inc., 2012.
- [7] P. G. Mongan, V. Modi, J. W. McLaughlin, E. P. Hinchy, R. M. O’Higgins, N. P. O’Dowd, C. T. McCarthy, Multi-objective optimisation of ultrasonically welded dissimilar joints through machine learning, *Journal of Intelligent Manufacturing* 33 (2022) 1125–1138. doi:[10.1007/s10845-022-01911-6](https://doi.org/10.1007/s10845-022-01911-6).



- [8] X. Liu, C. E. Athanasiou, N. P. Padture, B. W. Sheldon, H. Gao, A machine learning approach to fracture mechanics problems, *Acta Materialia* 190 (2020) 105–112. doi:[10.1016/j.actamat.2020.03.016](https://doi.org/10.1016/j.actamat.2020.03.016).
- [9] J. Hegde, B. Rokseth, Applications of machine learning methods for engineering risk assessment – A review, *Safety Science* 122 (2020) 104492. doi:[10.1016/j.ssci.2019.09.015](https://doi.org/10.1016/j.ssci.2019.09.015).
- [10] I. Dewancker, M. McCourt, S. Clark, Bayesian Optimization for Machine Learning : A Practical Guidebook, *arXiv:1612.04858 [cs]* (2016). [arXiv:1612.04858](https://arxiv.org/abs/1612.04858).
- [11] F. Ghavamian, Accelerating finite element analysis using machine learning (2021). doi:[10.4233/uuid:015bbf35-5e29-4630-b466-1a29d4c5bfb3](https://doi.org/10.4233/uuid:015bbf35-5e29-4630-b466-1a29d4c5bfb3).
- [12] S. Ryan, J. Berk, S. Rana, B. McDonald, S. Venkatesh, A bayesian optimisation methodology for the inverse derivation of viscoplasticity model constants in high strain-rate simulations, *Defence Technology* 18 (2022) 1563–1577. doi:[10.1016/j.dt.2021.10.013](https://doi.org/10.1016/j.dt.2021.10.013).
- [13] Y. Zhang, D. W. Apley, W. Chen, Bayesian Optimization for Materials Design with Mixed Quantitative and Qualitative Variables, *Scientific Reports* 10 (2020) 1–13. doi:[10.1038/s41598-020-60652-9](https://doi.org/10.1038/s41598-020-60652-9).
- [14] T. R. C. Chuaqui, A. T. Rhead, R. Butler, C. Scarth, A data-driven Bayesian optimisation framework for the design and stacking sequence selection of increased notched strength laminates, *Composites Part*

- B: Engineering 226 (2021) 109347. doi:[10.1016/j.compositesb.2021.109347](https://doi.org/10.1016/j.compositesb.2021.109347).
- [15] A. Borowska, H. Gao, A. Lazarus, D. Husmeier, Bayesian optimisation for efficient parameter inference in a cardiac mechanics model of the left ventricle, *International Journal for Numerical Methods in Biomedical Engineering* 38 (2022) e3593. doi:[10.1002/cnm.3593](https://doi.org/10.1002/cnm.3593).
- [16] H. Wankerl, C. Wiesmann, L. Kreiner, R. Butendeich, A. Luce, S. Sobczyk, M. L. Stern, E. W. Lang, Directional emission of white light via selective amplification of photon recycling and Bayesian optimization of multi-layer thin films, *Scientific Reports* 12 (2022) 5226. doi:[10.1038/s41598-022-08997-1](https://doi.org/10.1038/s41598-022-08997-1).
- [17] B. Gunn, I. T. Hettiarachchi, M. Johnstone, V. Le, D. Creighton, L. Preston, Improving high value manufacturing with simulation-based Bayesian Optimisation, in: *2022 IEEE International Systems Conference (SysCon)*, 2022, pp. 1–8. doi:[10.1109/SysCon53536.2022.9773798](https://doi.org/10.1109/SysCon53536.2022.9773798).
- [18] M. Abendroth, M. Kuna, Identification of ductile damage and fracture parameters from the small punch test using neural networks, *Engineering Fracture Mechanics* 73 (2006) 710–725. doi:[10.1016/j.engfracmech.2005.10.007](https://doi.org/10.1016/j.engfracmech.2005.10.007).
- [19] D. Chen, Y. Li, X. Yang, W. Jiang, L. Guan, Efficient parameters identification of a modified GTN model of ductile fracture using machine

- learning, *Engineering Fracture Mechanics* 245 (2021) 107535. doi:[10.1016/j.engfracmech.2021.107535](https://doi.org/10.1016/j.engfracmech.2021.107535).
- [20] W. C. Young, R. Budynas, *Roark's Formulas for Stress and Strain* (7th Edition), McGraw-Hill Professional Publishing, New York, USA, UNITED STATES, 2001.
- [21] W. Wcislik, Experimental determination of critical void volume fraction  $f_F$  for the Gurson Tvergaard Needleman (GTN) model, *Procedia Structural Integrity* 2 (2016) 1676–1683. doi:[10.1016/j.prostr.2016.06.212](https://doi.org/10.1016/j.prostr.2016.06.212).
- [22] V. Tvergaard, A. Needleman, Analysis of the cup-cone fracture in a round tensile bar, *Acta Metallurgica* 32 (1984) 157–169. doi:[10.1016/0001-6160\(84\)90213-X](https://doi.org/10.1016/0001-6160(84)90213-X).
- [23] B. Shahriari, K. Swersky, Z. Wang, R. P. Adams, N. de Freitas, Taking the Human Out of the Loop: A Review of Bayesian Optimization, *Proceedings of the IEEE* 104 (2016) 148–175. doi:[10.1109/JPROC.2015.2494218](https://doi.org/10.1109/JPROC.2015.2494218).
- [24] C. E. Rasmussen, C. K. I. Williams, *Gaussian Processes for Machine Learning*, Adaptive Computation and Machine Learning, MIT Press, Cambridge, Mass, 2006.
- [25] C. E. Rasmussen, *Gaussian Processes in Machine Learning*, in: O. Bousquet, U. von Luxburg, G. Rätsch (Eds.), *Advanced Lectures on Machine Learning: ML Summer Schools 2003*, Canberra, Australia, February 2 - 14, 2003, Tübingen, Germany, August 4 - 16, 2003, Revised Lectures,

- Lecture Notes in Computer Science, Springer, Berlin, Heidelberg, 2004, pp. 63–71. doi:[10.1007/978-3-540-28650-9\\_4](https://doi.org/10.1007/978-3-540-28650-9_4).
- [26] J. Wang, An Intuitive Tutorial to Gaussian Processes Regression, 2022. [arXiv:2009.10862](https://arxiv.org/abs/2009.10862).
  - [27] C. Zhu, R. H. Byrd, P. Lu, J. Nocedal, Algorithm 778: L-BFGS-B: Fortran subroutines for large-scale bound-constrained optimization, *ACM Transactions on Mathematical Software* 23 (1997) 550–560. doi:[10.1145/279232.279236](https://doi.org/10.1145/279232.279236).
  - [28] R. Kiran, K. Khandelwal, Gurson model parameters for ductile fracture simulation in ASTM A992 steels, *Fatigue & Fracture of Engineering Materials & Structures* 37 (2014) 171–183. doi:[10.1111/ffe.12097](https://doi.org/10.1111/ffe.12097).
  - [29] E. D. Meade, Experimental Study & Multiscale Modelling of the High Temperature Deformation of P91 under Multiaxial Loading, Ph.D. thesis, University of Limerick, 2020.
  - [30] D. Systemes, Abaqus/CAE User’s Guide - SIMULIA User Assistance 2021, Dassault Systemes, 2021.
  - [31] F. Pedregosa, G. Varoquaux, A. Gramfort, V. Michel, B. Thirion, O. Grisel, M. Blondel, P. Prettenhofer, R. Weiss, V. Dubourg, J. Vanderplas, A. Passos, D. Cournapeau, M. Brucher, M. Perrot, É. Duchesnay, Scikit-learn: Machine Learning in Python, *Journal of Machine Learning Research* 12 (2011) 2825–2830.
  - [32] G. De Ath, R. M. Everson, A. A. M. Rahat, J. E. Fieldsend, Greed is

- Good: Exploration and Exploitation Trade-offs in Bayesian Optimisation, *ACM Transactions on Evolutionary Learning and Optimization* 1 (2021) 1–22. doi:[10.1145/3425501](https://doi.org/10.1145/3425501). [arXiv:1911.12809](https://arxiv.org/abs/1911.12809).
- [33] M. Uy, J. K. Telford, Optimization by Design of Experiment techniques, in: 2009 IEEE Aerospace Conference, 2009, pp. 1–10. doi:[10.1109/AERO.2009.4839625](https://doi.org/10.1109/AERO.2009.4839625).
- [34] S. Fraley, M. Oom, B. Terrien, J. Zalewski, 14.1: Design of Experiments via Taguchi Methods - Orthogonal Arrays, in: *Chemical Process Dynamics and Controls*, 2020.
- [35] A. N. O’Connor, C. M. Davies, S. J. Garwood, The influence of constraint on fracture toughness: Comparing theoretical T0 shifts in master curve analyses with experimental data, *Engineering Fracture Mechanics* 275 (2022) 108857. doi:[10.1016/j.engfracmech.2022.108857](https://doi.org/10.1016/j.engfracmech.2022.108857).
- [36] M. Abbasi, M. Ketabchi, H. Izadkhah, D. H. Fatmehsaria, A. N. Aghbash, Identification of GTN model parameters by application of response surface methodology, *Procedia Engineering* 10 (2011) 415–420. doi:[10.1016/j.proeng.2011.04.070](https://doi.org/10.1016/j.proeng.2011.04.070).
- [37] G. Rousselier, Modeling of Plasticity and Ductile Fracture Physical Mechanisms and Numerical Simulation of Laboratory Specimens, Technical Report, 2019.
- [38] R. Yan, H. Xin, M. Veljkovic, Ductile fracture simulation of cold-formed high strength steel using GTN damage model, *Journal of Constructional Steel Research* 184 (2021) 106832. doi:[10.1016/j.jcsr.2021.106832](https://doi.org/10.1016/j.jcsr.2021.106832).

- [39] V. Tvergaard, Influence of voids on shear band instabilities under plane strain conditions, *International Journal of Fracture* 17 (1981) 389–407. doi:[10.1007/BF00036191](https://doi.org/10.1007/BF00036191).
- [40] W. Brocks, D. Klingbeil, G. Künecke, D.-Z. Sun, Application of the Gurson Model to Ductile Tearing Resistance, in: A. Bakker (Ed.), *Constraint Effects in Fracture Theory and Applications: Second Volume*, ASTM International, West Conshohocken, PA, 1995, pp. 232–252. doi:[10.1520/STP14638S](https://doi.org/10.1520/STP14638S).
- [41] A. O'Connor, P. Mongan, N. O'Dowd, A Machine Learning Approach to Automate Ductile Damage Parameter Selection in Finite Element Simulations, 2023. doi:[10.5281/zenodo.7620179](https://doi.org/10.5281/zenodo.7620179).